The Astrophysical Journal, 893:98 (13pp), 2020 April 20 https://doi.org/10.3847/1538-4357/ab7db1

An Ejecta Kinematics Study of Kepler's Supernova Remnant with High-resolution Chandra HETG Spectroscopy

Matthew J. Millard[1], Jayant Bhalerao[1], Sangwook Park[1], Toshiki Sato[2,3,4], John P. Hughes[5], Patrick Slane[6], Daniel Patnaude[7], David Burrows[8], and Carles Badenes[9,10]
[1] Box 19059, Department of Physics, University of Texas at Arlington, Arlington, TX 76019, USA
[2] RIKEN, 2-1 Hirosawa, Wako, Saitama 351-0198, Japan
[3] NASA, Goddard Space Flight Center, 8800 Greenbelt Road, Greenbelt, MD 20771, USA
[4] Department of Physics, University of Maryland Baltimore County, 1000 Hilltop Circle, Baltimore, MD 21250, USA
[5] Department of Physics and Astronomy, Rutgers University, 136 Frelinghuysen Road, Piscataway, NJ 08854-8019, USA
[6] Harvard-Smithsonian Center for Astrophysics, 60 Garden Street, Cambridge, MA 02138, USA
[7] Smithsonian Astrophysical Observatory, Cambridge, MA 02138, USA
[8] Dept. of Astronomy & Astrophysics, Penn State University, University Park, PA 16802 USA
[9] Department of Physics and Astronomy and Pittsburgh Particle Physics, Astrophysics and Cosmology Center (PITT PACC), University of Pittsburgh, 3941 O'Hara Street, Pittsburgh, PA 15260, USA
[10] Institut de Ciències del Cosmos (ICCUB), Universitat de Barcelona (IEEC-UB), Martí Franqués 1, E-08028 Barcelona, Spain
Received 2019 May 10; revised 2020 February 26; accepted 2020 March 6; published 2020 April 20

Abstract

We report our measurements of the bulk radial velocity from a sample of small, metal-rich ejecta knots in Kepler's supernova remnant (SNR). We measure the Doppler shift of the He-like Si Kα line-center energy in the spectra of these knots based on our Chandra High-Energy Transmission Grating Spectrometer observation to estimate their radial velocities. We estimate high radial velocities of up to $\sim$8000 km s^{-1} for some of these ejecta knots. We also measure proper motions for our sample based on the archival Chandra Advanced CCD Imaging Spectrometer data taken in 2000, 2006, and 2014. Our measured radial velocities and proper motions indicate that some of these ejecta knots are almost freely expanding after $\sim$400 yr since the explosion. The fastest moving knots show proper motions of up to $\sim 0\farcs2$ per year. Assuming that these high-velocity ejecta knots are traveling ahead of the forward shock of the SNR, we estimate the distance to Kepler's SNR $d \sim 4.4$–7.5 kpc. We find that the ejecta knots in our sample have an average space velocity of $v_s \sim 4600$ km s^{-1} (at a distance of 6 kpc). We note that 8 of the 15 ejecta knots from our sample show a statistically significant (at the 90% confidence level) redshifted spectrum, compared to only two with a blueshifted spectrum. This may suggest an asymmetry in the ejecta distribution in Kepler's SNR along the line of sight; however, a larger sample size is required to confirm this result.

Unified Astronomy Thesaurus concepts: Supernova remnants (1667); Interstellar dynamics (839); Proper motions (1295); X-ray astronomy (1810); Radial velocity (1332)

1. Introduction

Type Ia supernovae (SN Ia) are most likely the result of the unbinding of a white dwarf that has accreted enough mass from a companion, either through a merger or matter stream (Iben & Tutukov 1984), to burn carbon and oxygen (Hoyle & Fowler 1960), resulting in a runaway thermonuclear explosion. The evolution of Type Ia supernova remnants (SNRs) may be modeled assuming a uniform interstellar medium interaction (Badenes et al. 2007; Martínez-Rodríguez et al. 2018). However, asymmetries in ejecta distributions have been seen in some Type Ia SNRs (e.g., Uchida et al. 2013; Post et al. 2014), indicating that the explosion environment is likely more complex. The explosion itself might not have been spherically symmetric (e.g., Kasen et al. 2009; Maeda et al. 2010, 2011), and the initial non-uniformity in the SN ejecta may be caused by such an explosion asymmetry. If the white dwarf is interacting with a non-degenerate companion star, the disk that would likely form around the accreting white dwarf may produce a wind that could strip material from the companion, creating an anisotropic circumstellar medium (CSM; e.g., Hachisu et al. 2008) surrounding the progenitor system. Such a modified medium could contain regions of varying density, which may slow down some of the ejecta from the SN explosion, while leaving other parts of the ejecta gas unaffected.

A well-known case where a Type Ia SNR is interacting with CSM is the remnant of SN 1604, or Kepler's SNR (Kepler hereafter), the most recent Galactic historical supernova. As a young, ejecta-dominated remnant of a luminous (assuming a distance >7 kpc) SN Ia (Patnaude et al. 2012) from a metal-rich progenitor (Park et al. 2013), it provides an excellent opportunity to study the nature of a Type Ia progenitor and its explosion in the presence of CSM material (Burkey et al. 2013) and nitrogen-rich gas (Dennefeld 1982; Blair et al. 1991; Katsuda et al. 2015). Strong silicate dust features observed in the infrared spectra of the remnant are indicative of the wind from an oxygen-rich asymptotic giant branch star (Williams et al. 2012). The distance to Kepler's SNR is uncertain; recent estimates put the distance from 3.9 kpc (Sankrit et al. 2005) to $\gtrsim$7 kpc (Chiotellis et al. 2012; Patnaude et al. 2012).

In X-rays, Kepler appears as mostly circular with an angular diameter of $\sim 3\farcm6$; however, it does have curious morphological features. For example, there are two notable protrusions located in the east and west portion of the SNR, often referred to as "Ears" (Tsebrenko & Soker 2013; a similar case is G299.2-2.9 Post et al. 2014). Kepler also shows emission features from shocked CSM, one located across the center of the remnant and another that stretches across the northern rim (Burkey et al. 2013). Park et al. (2013) found a higher Ni to Fe K line flux ratio in the northern half than in the southern half of Kepler, but

were not able to distinguish the origin for the differential Ni/Fe flux ratio (shock interactions with different CSM densities between the north and south versus an intrinsically different ejecta distribution between the north and south). Katsuda et al. (2008) found that the northern half was expanding more slowly than the southern half, suggesting an uneven ejecta distribution between the northern and southern shells, although they attributed the difference to interaction with a dense CSM in the north.

Measuring the Doppler shifts in the emission lines from the X-ray-emitting ejecta knots projected over the face of the SNR, and thus their bulk motion line of sight ("radial" hereafter) velocities (v_r) is useful to reveal the 3D structure of the clumpy ejecta gas. The velocity measurements of these knots may help to reveal the ejecta properties immediately after the explosion, as well as their interaction with the CSM, which was formed by the progenitor system's mass-loss history. Sato & Hughes (2017b) reported measurements of radial velocity for several compact X-ray-bright knots in Kepler's SNR using archival Chandra Advanced CCD Imaging Spectrometer (ACIS) data. They measured high radial velocities of up to $\sim 10^4$ km s^{-1} and nearly free-expansion rates for some knots.

Here, we present the results of our study on 3D velocity measurements of a sample of 17 small, bright regions in Kepler, based on high-resolution X-ray spectroscopy from our Chandra High-Energy Transmission Grating Spectrometer (HETGS) observation. In Section 2 we present the observations we used for our analysis. In Section 3 we show our analysis techniques and results. In Section 4 we estimate the distance to Kepler and discuss its ejecta distribution based on our results, and in Section 5 we summarize our findings.

2. Observations

We performed our Chandra HETGS observation of Kepler using the ACIS-S array from 2016 July 20 to 2016 July 23. The aim point was set at R.A.(J2000) = $17^{\rm h}30^{\rm m}41\overset{\rm s}{.}3$, Dec (J2000) = $-21°29'28\overset{''}{.}9$, roughly toward the geometric center of the SNR. The observation was composed of a single ObsID, 17901. We processed the raw event files using Chandra Interactive Analysis of Observations (CIAO; Fruscione et al. 2006) version 4.10 and the Chandra Calibration Database (CALDB) version 4.7.8 to create a new level=2 event file using the CIAO command, `chandra_repro`. Next, we removed time intervals of background flaring using the Chandra Imaging and Plotting System (ChIPS) command, `lc_sigma_clip`, which left us with a total effective exposure of 147.6 ks. We then extracted the first-order dispersed spectra from a number of small regions across the SNR (Section 3.2) using the TGCat scripts (Huenemoerder et al. 2011) `tg_create_mask`, `tg_resolve_events`, and `tgextract`, and also created appropriate detector response files. The TGCat commands (in the order mentioned) first create a FITS region file that specifies a region position, shape, size, and orientation in sky pixel-plane coordinates.[11] Next, event positions are compared with the 3D locations at which dispersed photons can appear, given the grating equation and zero-order position, and TGCat assigns them a wavelength and an order, and outputs these data into a grating events file.[12] Finally, the grating events file is filtered and binned into a one-dimensional counts spectrum for each grating part, order, and source.[13] In addition to our new HETGS data, we also used the archival ACIS data of Kepler as supplementary data (listed in Table 1). For spectral fitting purposes (Section 3.3), we reprocessed the six ObsIDs from the 2006 archival ACIS-S3 data by following standard data reduction procedures with CIAO versions 4.8–4.8.2 and CALDB version 4.7.2, which resulted in a total effective exposure of ~733 ks. To make our proper motion measurements, we used the 2000, 2006, and 2014 archival Chandra ACIS data, as previously processed and prepared in Sato & Hughes (2017b).

Table 1
Archival Chandra ACIS Observations

Observation ID	Start Date	Exposure Time (ks)
116	2000 Jun 30	48.8
4650	2004 Oct 26	46.2
6714	2006 Apr 27	157.8
6715	2006 Aug 3	159.1
6716	2006 May 5	158.0
6717	2006 Jul 13	106.8
6718	2006 Jul 21	107.8
7366	2006 Jul 16	51.5
16004	2014 May 13	102.7
16614	2014 May 16	36.4

3. Data Analysis and Results

3.1. Utility of HETGS for Extended Sources

Due to its dispersed nature, the Chandra HETGS (the first-order) is best suited to measure the spectra of isolated, point-like sources. The utility of the HETG spectrum is affected when the source is extended and/or surrounded by complex background emission features. Our study of Kepler is typical of such a case; the SNR comprises many small, discrete extended sources projected against its own complex diffuse emission. The HETG-dispersed image of Kepler is shown in Figure 1. Our goal is to measure the atomic line-center energies in the X-ray emission spectrum for small individual emission features within the SNR. For this type of measurement, the utility of HETG data have been successfully demonstrated by previous authors in the cases of Cassiopeia A (Cas A; Lazendic et al. 2006) and G292.0 + 1.8 (G292; Bhalerao et al. 2015). He-like Si Kα lines were used for Cas A, while He- and H-like Ne, Mg, and Si Kα lines were used for G292. In the integrated spectrum of Kepler, the Fe L and K, and He-like Si and S Kα lines are prominent. However, the Fe K line is faint in the spectra of individual small knots, and thus not useful for our study. Additionally, the Fe L lines are a complex composed of several closely spaced emission lines, which makes it difficult to identify them for Doppler shift measurements, whereas the He-like Si Kα and S He-like Kα lines each may easily be represented by a simple trio of emission lines. Overall, the ejecta knots in Kepler are fainter than those in Cas A and G292. Thus, the count statistics for most knots only allow us to use the brightest line, He-like Si Kα. In general, we found that at least ~100 counts for the He-like Si Kα line-emission features in the 1.75–1.96 keV band of the first-order Medium Energy Grating (MEG) spectrum of each individual target source are required to make a reliable Doppler shift measurement.

[11] http://cxc.harvard.edu/ciao/ahelp/tg_create_mask.html
[12] http://cxc.harvard.edu/ciao/ahelp/tg_resolve_events.html
[13] https://cxc.harvard.edu/ciao/ahelp/tgextract.html

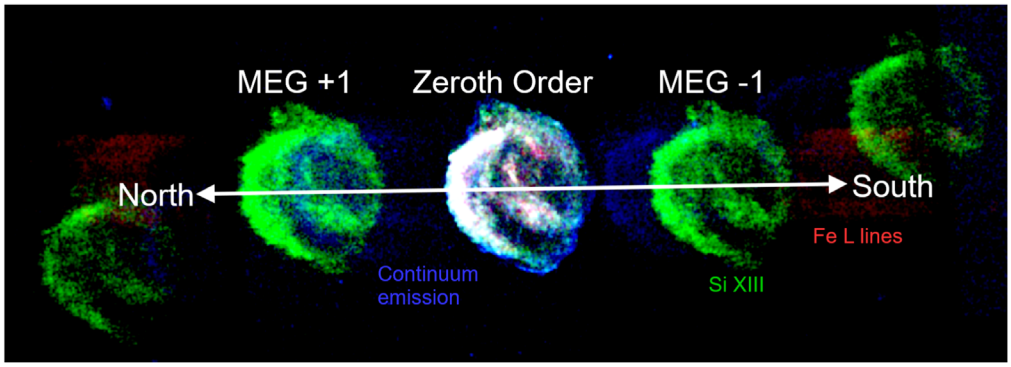

Figure 1. Chandra HETG 3-color image of Kepler. Red: 0.7–1.2 keV; green: 1.7–2.0 keV; and blue: 2.0–8.0 keV. The Fe L complex and continuum emission appear smeared across the ACIS-S chips, the former because it consists of many emission lines, and the latter because it lacks individual emission lines. The Si XIII (He-like Si Kα) emission is more focused on the detector, because it consists only of three closely spaced lines at ~1.865 keV.

Distinguishing the He-like Si Kα lines from the target emission knot from those of the surroundings is essential to correctly measure the line-center energies of He-like Si Kα lines in the spectrum of small individual knots in Kepler. To quantitatively assess the contamination in the He-like Si Kα line profiles of the target source from the nearby emission features, as well as due to the target source extent, we performed ray-trace simulations of Chandra observations using the Model of AXAF Response to X-rays (MARX) package (Davis et al. 2012). Initially, we assumed a point-like target source with an X-ray spectrum representing the rest-energy emission lines of He-like Si Kα, at various distances from the zeroth-order position. Figures 2(a) and (b) show that the first-order spectral lines (He-like Si Kα) are shifted from the true line-center energies as the source position is off-centered, corresponding to the Chandra HETGS wavelength scale of 0.0113 Å arcsec^{-1} for High Energy Grating and 0.0226 Å arcsec^{-1} for MEG.[14] Using this relation, we may identify interfering emission lines in our source spectra originating from nearby sources. We also tested how the angular extent of the target sources affect our line-center measurements. While larger source extents would increase the uncertainties in the line-center energy measurements, we conclude that our radial velocity measurements would not be affected (within uncertainties) as long as the target source sizes are $\lesssim$10″ (Figures 2(c) and (d)).

Based on our test simulations, we also conclude that nearby discrete sources positioned ~25″ or farther off the target source position along the dispersion direction would not affect our measurements of the source spectral line-center energies for radial velocities. For the cases where nearby sources are present (with angular extent similar to that of the target source) within ~25″ of the target source along the dispersion direction, the effects on the line-center measurements for the target source may vary. We investigated numerous source configurations (both with our actual data of Kepler and extensive MARX simulations), and found that even if the nearby source positions are relatively close to the target position, we may avoid a significant contamination from the nearby emission by adjusting the criteria for the selection of the first-order photons of the target spectrum via the "osort" parameters, *osort_lo* and *osort_hi*.[15] During HETG spectrum extraction, only photons with measured wavelengths that meet the criteria, $osort\_lo < \lambda_g/\lambda_{CCD} \leqslant osort\_hi$ are included in the first-order spectrum, where λ_{CCD} is the ACIS-S CCD wavelength, and λ_g is the gratings wavelength. Because λ_{CCD} and λ_g values of nearby sources become more divergent the farther they are located from the target position, photons from those nearby sources are less likely to be included in the extracted spectrum when small osort values are chosen. Thus, we may still be able to measure the source line-center energies despite the presence of nearby contaminating emission features. However, we find it unlikely that the emission lines from sources located very near each other ($\lesssim$5″) along the dispersion direction, with similar brightness, would be properly distinguishable.

3.2. Radial Velocities

Based on archival Chandra ACIS data (Table 1), we identified numerous small emission features that are bright in the 1.7–2.0 keV band, suggesting that they may be good candidate targets for He-like Si Kα line-center energy measurements using an HETG first-order spectrum. We selected 17 features (Figure 3), generally satisfying the criteria that we discussed in Section 3.1. To measure the v_r of these X-ray emission features projected within the boundary of Kepler's SNR, we adopt a method similar to those pioneered by Lazendic et al. (2006) and Bhalerao et al. (2015), who analyzed HETG spectra of bright X-ray knots in SNRs Cas A and G292, respectively. For each of these 17 individual features, we extracted the first-order spectrum from our Chandra HETGS observation.

For each extracted region, the line-center energies of the He-like Si Kα lines, and two Si XII emission lines (see below), were measured by fitting six Gaussian curves to the spectrum—three for He-like Si Kα, two for the Si XII emission lines, and one for the background continuum using the Interactive Spectral Interpretation System software package (Houck & Denicola 2000). The measured line-center wavelengths were then compared with the rest values (6.648 Å for resonance, 6.688 Å for intercombination, 6.740 Å for the forbidden line, and 6.717 Å and 6.782 Å for the Si XII lines, respectively Drake 1988), to measure the Doppler shifts in these lines, and thus to estimate the corresponding v_r.

The count statistics of our data do not allow us to directly measure the He-like Si (XIII) Kα intercombination to resonance (i/r) and forbidden to resonance (f/r) resonance line flux ratios. Thus, we use i/r and f/r ratios that correspond to the values that we measured for each knot using archival ACIS

[14] http://cxc.harvard.edu/proposer/POG/html/chap8.html
[15] See footnote 12.

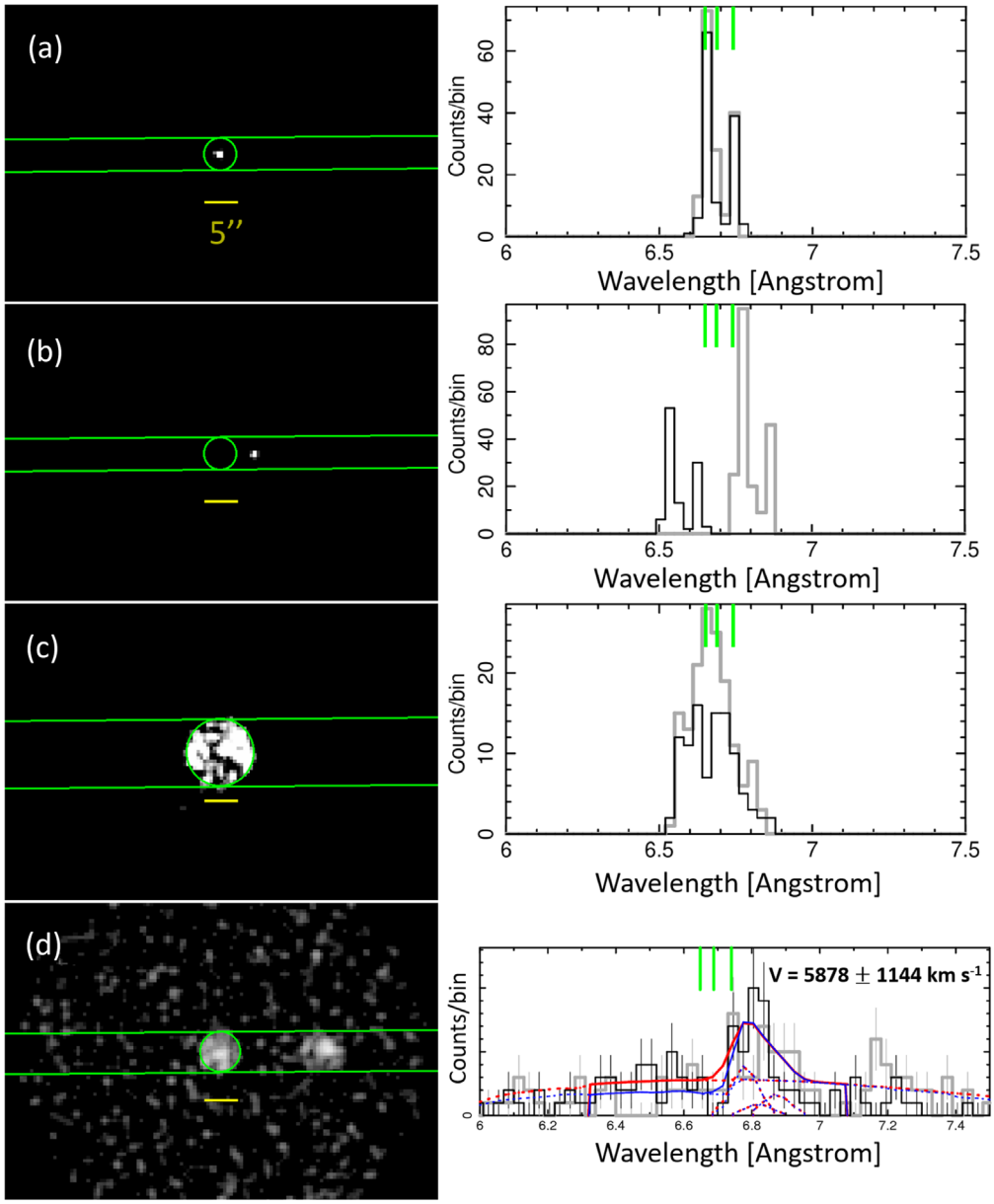

Figure 2. The left column shows images from our MARX simulations (assuming a Chandra HETGS + ACIS-S configuration). The green circle and horizontal lines show the target region, and dispersion direction, respectively. The yellow scale bar in each image is 5″ across. The right column shows the extracted first-order MEG spectrum. The black line and gray line are the plus and minus order spectrum, respectively. The rest energies of the He-like Si Kα line used here are 6.648, 6.688, and 6.740 Å, denoted by green vertical lines in panel (d). Panel (a) shows the spectrum of a point source, with the zeroth-order point centered on it. The plus and minus order spectra are aligned at the rest energy of the line trio when the source is located at the zeroth-order point. Panel (b) exhibits the effect of shifting the zeroth-order point by 5″ along the dispersion direction. The plus and minus orders move away from the line-center energy. Panel (c) shows an extended source (10″), which broadens the resulting peaks in the spectra. Panel (d) contains a complex source configuration. The target source has an angular size of 6″, and assumed radial velocity of $v_r = +6000$ km s^{-1}. The nearby source has an angular size of the 6″ and an assumed radial velocity of $v_r = +9000$ km s^{-1}. The assumed angular offset of the nearby source is 15″. Despite the proximity of the two sources, the correct Doppler shift was measured, $v_r = 5878 \pm 1144$ km s^{-1}, in part due to the appropriate choice of osort value (0.05 in this case). The red line and blue lines are the best-fit models for the +1 and −1 order spectra, respectively.

data (Section 3.3). At the temperatures and ionization timescales that we measure for the knots in our sample, Si XII emission lines at ∼6.717 and ∼6.782 Å may also contribute significantly to the spectrum. Thus, we account for these lines in our v_r fitting model. In the Appendix, we discuss the effects of varying line ratios on our v_r estimates. In general, the uncertainty in line ratio values does not affect our conclusions.

Our results are summarized in Table 2, with spectra and best-fit models shown in Figure 4. Errors represent a 90% confidence interval unless otherwise noted. Figure 3 shows the locations of blueshifted and redshifted regions, marked by cyan and red circles, respectively. Our measured v_r for two CSM regions (regions C2* and C4*) are negligible even though they are projected near the SNR center. This low v_r is perhaps as expected for the shocked CSM features regardless of their projected distance from the SNR center, supporting the reliability of our v_r measurements. Of the 15 ejecta knots for which we measured v_r, only 2 (N5 and Ear3) show a significantly blueshifted spectrum, while the other eight regional spectra are significantly redshifted.

We note that four ejecta knots in our sample (regions N2, N1, N3, and N7) were also studied in Sato & Hughes (2017b),

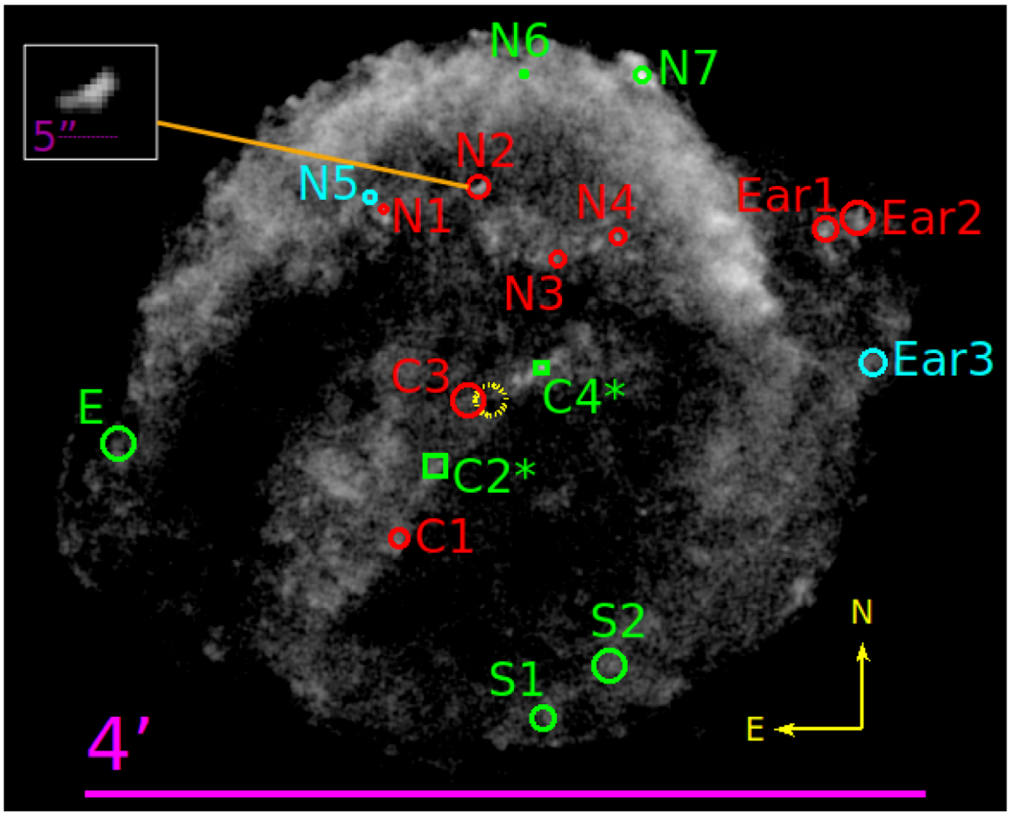

Figure 3. ACIS-S grayscale image of Kepler's SNR from the 2014 observation, filtered to the energy range 1.7–2.0 keV. Seventeen ejecta and CSM knots that we analyzed in this work are marked with circles. CSM knots are marked with squares (also, their region names include " * "). Otherwise, we identify all other knots to be metal-rich ejecta based on our spectral analysis of the archival ACIS data. Cyan and red markers indicate blue and redshifted features, respectively, while green represents statistically negligible v_r at the 90% confidence interval. The uncertainty in the kinematic center of the SNR estimated by Sato & Hughes (2017b) is denoted by a dotted yellow circle. A zoomed-in image of knot N2 is shown in the upper left corner.

who measured the v_r of these ejecta knots based on Chandra ACIS data. For three of these common regions, N2, N1, and N3, we measure high v_r values ($v_r \sim 5600$–7700 km s^{-1}). These regions are located in the northern shell of the SNR, approximately 1′ from the kinematic center (R.A.(J2000) = $17^{\rm h}30^{\rm m}41\overset{\rm s}{.}321$ and decl.(J2000) = $-21°29'30\overset{''}{.}51$ Sato & Hughes 2017b). For all four of our common knots, we find general agreement between our measured values and those from Sato & Hughes (2017b), as shown in Table 2. This is an interesting result when we consider that the v_r measurements based on the low-resolution ACIS spectrum are dominated by systematic uncertainties (∼500–2000 km s^{-1}) (Sato & Hughes 2017a, 2017b), while those using our high-resolution HETGS spectrum are mostly dominated by statistical uncertainties (due to the relatively lower throughput of the dispersed spectroscopy), yet our results for those four ejecta regions are consistent. Almost all other ejecta knots show significantly lower velocities of $v_r \lesssim 2300$ km s^{-1} (Table 2). It is notable that two ejecta knots (regions Ear1 and Ear2) projected within the western "Ear" region show a significant v_r (∼2200 and 900 km s^{-1}) even though they are projected far (∼2′) from the center of the remnant beyond the main shell of the SNR.

3.3. Identifying Metal-rich Ejecta

To identify the origin of small emission regions in our sample (metal-rich ejecta versus low-abundant CSM), we performed spectral model fits for each individual regional spectrum based on the archival Chandra ACIS data with the deepest exposure (combining all ObsIDs taken in 2006, with a total exposure of 733 ks). We fitted the observed 0.3–7.0 keV band ACIS spectrum extracted from each region with an absorbed X-ray emission spectral model assuming optically thin hot gas with non-equilibrium ionization (`phabs*vpshock` Borkowski et al. 2001) using the XSPEC software package (Arnaud 1996). We estimated the background spectrum with small faint diffuse emission regions nearby each source region within the SNR. Then, we subtracted the background spectrum from the source regional spectrum before the spectral model fitting. We allowed the electron temperature (kT, where k is the Boltzmann constant and T is electron temperature), ionization timescale (n_et: the electron density, n_e, multiplied by the time since being shocked, t), redshift, normalization, and abundances of O, Ne, Mg, Si, S, Ar, and Fe to vary in the spectral model fitting. We fixed all other elemental abundances at solar values (Wilms et al. 2000). We note that, although H and He are generally not expected to be abundant in the spectrum of ejecta-dominated emission features of Type Ia SNRs, Kepler is interacting with a significant amount of CSM. Thus, we leave the H and He abundances fixed at solar values in our model to account for possible CSM interaction throughout the SNR. In the ejecta-dominated knots, we also use the H and He continuum as an approximation for non-thermal power-law emission from the shock-accelerated electrons at the forward shock. We fixed the absorption column to $N_{\rm H} = 5.4 \times 10^{22}$ cm^{-2} (Foight et al. 2016). We found significant residuals at $E \sim 0.75$ and ∼1.25 keV in the spectra of the ejecta knots. Similar features have been noticed in

Table 2
Radial Velocity and Proper Motions of Small Emission Features in Kepler's SNR

Region[†]	R.A.[a] (degree)	Decl.[a] (degree)	D[b] (arcmin)	v_r (km s^{-1})	$v_{r(\mathrm{SH})}$[c] (km s^{-1})	$\mu_{\mathrm{R.A.}}$ (arcsec yr^{-1})	$\mu_{\mathrm{decl.}}$ (arcsec yr^{-1})	μ_{Tot}[d] (arcsec yr^{-1})	η[e]	v_s[f] (km s^{-1})
N2	262.67314	−21.474812	1.02	7684^{+1155}_{-1177}	9110^{+30}_{-110}	0.028 ± 0.017	0.137 ± 0.024	0.140 ± 0.029	0.94 ± 0.14	8656^{+1093}_{-1112}
N1	262.68120	−21.476634	1.04	6019^{+1294}_{-1385}	8700^{+650}_{-470}	−0.065 ± 0.016	0.081 ± 0.024	0.104 ± 0.028	0.68 ± 0.10	6707^{+1213}_{-1291}
N3	262.66648	−21.480553	0.74	5550^{+2253}_{-2172}	5880^{+690}_{-1750}	0.045 ± 0.016	0.078 ± 0.024	0.090 ± 0.028	0.83 ± 0.16	6113^{+2073}_{-2000}
C3	262.67403	−21.491796	0.10	2281^{+1449}_{-1337}	⋯	0.019 ± 0.018	−0.021 ± 0.024	0.028 ± 0.03	1.86 ± 2.64	2416^{+1397}_{-1293}
N4	262.66124	−21.478912	0.98	2252^{+1761}_{-1664}	⋯	0.061 ± 0.017	0.105 ± 0.027	0.121 ± 0.032	0.85 ± 0.13	4115^{+1229}_{-1187}
Ear1	262.64352	−21.478218	1.79	2180^{+778}_{-752}	⋯	0.067 ± 0.016	0.059 ± 0.024	0.089 ± 0.029	0.34 ± 0.03	3342^{+806}_{-795}
C1	262.67997	−21.502758	0.79	1823^{+1408}_{-1458}	⋯	−0.058 ± 0.017	−0.064 ± 0.024	0.086 ± 0.029	0.75 ± 0.14	3052^{+1070}_{-1094}
Ear2	262.64087	−21.477378	1.95	942^{+525}_{-546}	⋯	0.172 ± 0.017	0.104 ± 0.024	0.201 ± 0.029	0.71 ± 0.05	5798^{+819}_{-819}
N6	262.66920	−21.465973	1.56	883^{+954}_{-933}	⋯	0.002 ± 0.018	0.141 ± 0.024	0.141 ± 0.03	0.62 ± 0.06	4109^{+859}_{-858}
E	262.70386	−21.495295	1.78	531^{+1551}_{-1269}	⋯	−0.171 ± 0.016	-0.051 ± 0.024	0.179 ± 0.029	0.69 ± 0.06	5122^{+837}_{-831}
C2[g]	262.67685	−21.497011	0.41	-175^{+672}_{-700}	⋯	−0.047 ± 0.016	−0.013 ± 0.024	0.049 ± 0.028	0.83 ± 0.30	1406^{+795}_{-796}
N7	262.65918	−21.466017	1.71	-225^{+382}_{-398}	244^{+46}_{-10}	0.026 ± 0.015	0.026 ± 0.023	0.037 ± 0.028	0.15 ± 0.01	1077^{+783}_{-784}
C4[g]	262.66782	−21.489190	0.29	-233^{+803}_{-862}	⋯	0.004 ± 0.015	0.004 ± 0.023	0.006 ± 0.028	0.14 ± 0.07	289^{+801}_{-840}
S1	262.66758	−21.517109	1.54	-246^{+897}_{-882}	⋯	−0.033 ± 0.018	-0.070 ± 0.024	0.077 ± 0.03	0.34 ± 0.03	2205^{+854}_{-854}
S2	262.66207	−21.512892	1.38	-536^{+1060}_{-1067}	⋯	0.058 ± 0.017	-0.120 ± 0.024	0.133 ± 0.029	0.66 ± 0.07	3823^{+831}_{-831}
Ear3	262.63949	−21.488767	1.83	-2239^{+1087}_{-973}	⋯	0.140 ± 0.016	0.018 ± 0.024	0.141 ± 0.03	0.53 ± 0.04	4595^{+915}_{-884}
N5	262.68243	−21.475636	1.13	-6716^{+1535}_{-1613}	⋯	−0.054 ± 0.018	0.077 ± 0.024	0.094 ± 0.03	0.57 ± 0.07	7229^{+1461}_{-1531}

Notes.
[a] Position in 2016 (J2000).
[b] Projected angular distance from kinematic center estimated by Sato & Hughes (2017b), R.A.(J2000) = $17^{\mathrm{h}}30^{\mathrm{m}}41\overset{\mathrm{s}}{.}321$ and decl.(J2000) = $-21°29'30\overset{''}{.}51$, with uncertainties of $\sigma_{\mathrm{R.A.}} = \pm 0\overset{'}{.}073$ and $\sigma_{\mathrm{decl.}} = \pm 0\overset{'}{.}072$, respectively.
[c] Values taken from Sato & Hughes (2017b). Errors represent a 68% confidence interval.
[d] $\mu_{\mathrm{Tot}} = \sqrt{\mu^2_{\mathrm{R.A.}} + \mu^2_{\mathrm{decl.}}}$.
[e] Expansion index (see Section 3.4).
[f] Estimated space velocity for a distance of 6 kpc.
[g] CSM-dominated knot.

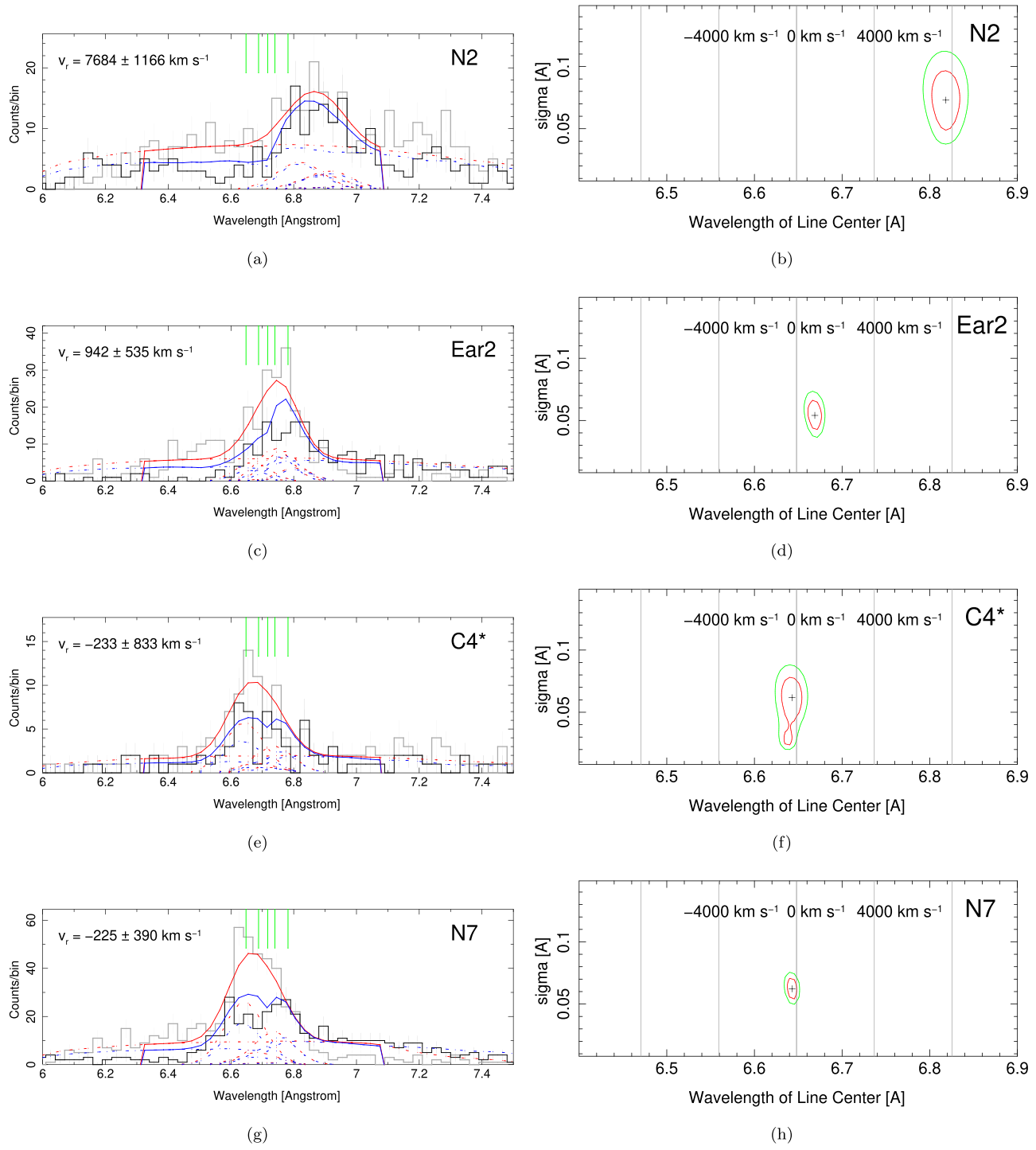

Figure 4. Examples of our line-center energy fits for small emission features in Kepler. The left column is the HETG spectra overlaid with the best-fit model. The straight green lines show the locations of the rest-frame He-like Si Kα line-center wavelengths. The dashed lines show individual Gaussian components of our best-fit model. The errors represent a 90% confidence interval. Gray: MEG +1 data; black: MEG −1 data; red: MEG +1 model fit; blue: MEG −1 model fit. The right column shows the confidence level contours for the best-fit v_r value. The red and green contours represent a 68% and 90% confidence interval, respectively. Panels (a–b) and (c–d) are from regions N2 and Ear2, respectively, showing clearly redshifted spectra. Panels (e–f) and (g–h) are from regions C4* and N7, respectively, showing negligible Doppler shift.

several other SNR studies of ejecta-dominated (particularly Fe-rich) spectra (Hwang et al. 1998; Katsuda et al. 2015; Sato & Hughes 2017b; Yamaguchi et al. 2017). To improve our spectral model fits, we added Gaussian components at these energies to account for these emission line features of the ejecta knot spectra (adding these Gaussian components does not significantly improve the spectral model fit of the CSM-dominated regions, and thus, were not included in those fits). We note that this implementation is not physically motivated, and is only intended as a statistical improvement in the spectral model fits. We confirm that excluding these Gaussians does not affect our conclusions (distinguishing between ejecta-

dominated and CSM-dominated regions, as discussed later). Our reduced chi-squared values for the best-fit models range from $\chi^2_\nu = 1.0$–1.4.

Given that Si and Fe are the most efficiently produced elements in a Type Ia explosion, we identified our knots as CSM-dominated or ejecta-dominated based on our measured abundances of Si and Fe. Knots with low Si and Fe abundances relative to solar values, $[\mathrm{Si/Si_\odot}] \lesssim 1.5$ and $[\mathrm{Fe/Fe_\odot}] \lesssim 1$, were deemed CSM-dominated, while those that have an enhanced abundance $[\mathrm{Si/Si_\odot}] \gtrsim 3$, and $[\mathrm{Fe/Fe_\odot}] > 1$, were classified as ejecta-dominated. This way, we identified 15 knots as ejecta-dominated and 2 as CSM-dominated. The best-fit electron temperatures of nearly all ejecta knots in our sample are $kT \sim 2$–5 keV, with ionization timescales $n_e t \sim (1\text{–}3) \times 10^{10}$ cm^{-3} s. The medians of these best-fit kT and $n_e t$ ejecta values generally agree with the higher-temperature ejecta components measured by Katsuda et al. (2015). For three ejecta-dominated knots, S2, N7, and Ear1, and for the CSM-dominated knots, we measure lower temperatures ($kT \sim 0.5$–1.3 keV) and higher ionization timescales ($n_e t \sim 5 \times 10^{10}$–$10^{12}$ cm^{-3} s). We attribute the outlying kT and $n_e t$ observed in these three ejecta knots to possible CSM interaction. The spectral fitting results are summarized in Table A1 in the Appendix.

3.4. Proper Motions

Based on the archival Chandra ACIS data covering the net time span of 14 yr (2000–2014, Table 1), we estimate the proper motions of the small ejecta regions for which we measure v_r. To measure the proper motions, we apply the methods used in Sato et al. (2018). We took the image from the long observation in 2006 as the reference "model" for each knot, compared it to the images from other epochs by incrementally shifting it in R.A. and decl., and then calculated the value of the Cash statistic (Cash 1979),

$$C = -2\sum_{i,j}(n_{i,j}\ln m_{i,j} - m_{i,j} - \ln n_{i,j}!), \quad (1)$$

where $n_{i,j}$ and $m_{i,j}$ are the number of counts in the ith, jth pixels from the current epoch, and in 2006, respectively, scaled by the total number of counts in the SNR. When the Cash statistic reached a minimum value, it meant the pixel values in the image for each "test" epoch most closely matched those found in the reference image, indicating that its position in the test epoch was determined. We estimate the error in the parameters using $\Delta C = C - C_{\min}$, which may be interpreted in a way similar to $\Delta\chi^2$, and also include the systematic image alignment uncertainty from each epoch (Sato & Hughes 2017b). The results of our proper motion measurements are summarized in Table 2. Our measured proper motions range from $\mu_{\mathrm{R.A.}} \sim -0.''17$ to $0.''17$ yr^{-1} in R.A. and $\mu_{\mathrm{decl.}} \sim -0.''12$ to $0.''14$ yr^{-1} in decl. Figure 5 shows zoomed-in images of knots, demonstrating their positional changes over 14 yr. Knot Ear2, projected within the western Ear of Kepler, shows the largest proper motion, $\mu_{\mathrm{Tot}} \sim 0.''20$ yr^{-1}, which is perhaps as expected, considering that it is an ejecta knot projected beyond the main shell of Kepler. The CSM-dominated regions generally show negligible proper motions, which may also be expected.

Sato & Hughes (2017b) found that ejecta knots with the highest v_r (N2, N1, N3) tend to show proper motions close to their extrapolated time-averaged rates for the change of angular positions, μ_{Avg} (their angular distance from the SNR center estimated by Sato & Hughes (2017b) divided by the age of Kepler, 412 yr as of 2016), suggesting that they have not undergone significant deceleration since the explosion (i.e., they are nearly freely expanding). From here on we refer to $\mu_{\mathrm{Tot}}/\mu_{\mathrm{Avg}}$ as the expansion index, η. If an ejecta knot has been moving undecelerated since the explosion, we may expect $\eta \approx 1$. We find several ejecta knots to have an expansion index close to 1 ($\eta \gtrsim 0.7$, see Table 2). We note that region C3 is an anomaly with $\eta = 1.86$. This discrepancy is probably due to its projected proximity to the SNR center. The angular offset of C3 from the SNR center is similar to the uncertainties on the SNR center position, and, in fact, η is not constrained (Table 2). Knot C2* also shows a high η value, and is projected near the center of the SNR with a large uncertainty in η (± 0.3). Its spectrum is clearly CSM-dominated and its low proper motion is consistent with a CSM origin. In general, CSM-dominated regions are not expected to have a high η value. The source of this discrepancy is unclear; however, we speculate that this dense filament of CSM-dominated gas may have been ejected from the progenitor system shortly before the SN explosion took place. Thus, like other parts of the remnant, it has possibly only been traveling for ~400 yr.

4. Discussion

4.1. Distance to Kepler

The kinematic nature of ejecta knot N2 in Kepler is remarkable. Sato & Hughes (2017b) measured an expansion index $\eta \sim 1$, indicating that it is almost freely expanding. Here, we measure a similarly high expansion index, and a high v_r (nearly 8000 km s^{-1}). In general, X-ray-emitting ejecta features in SNRs are expected to be heated to $T > 10^6$ K by the reverse shock, being somewhat decelerated in the process. To explain the existence of nearly freely expanding ejecta knots in Kepler, Sato & Hughes (2017b) used the findings from Wang & Chevalier (2001) to argue that these ejecta knots may have survived to the current age of Kepler (~400 yr) if their initial density contrast to the surrounding medium was high (≳100). Alternatively, they suggested that the highly structured environment of the remnant contains low-density ($n_{\mathrm{H}} \sim 0.1$ cm^{-3}) "windows" through which some ejecta knots may have traveled. This causes a late encounter with the reverse shock, allowing for the survivability of lower density contrast, nearly undecelerated knots to the forward shock region, according to the simulations of Wang & Chevalier (2001). This is the scenario favored by Sato & Hughes (2017b). Either scenario may be applied in the interpretation of our results. Considering that Kepler is located hundreds of parsecs out of the Galactic plane where the ambient density is $n_{\mathrm{H}} \lesssim 0.01$ cm^{-3} (McKee & Ostriker 1977), the existence of low-density regions around the SN site appears to be plausible.

Since we know the exact age of the SNR, and we have measured the radial velocity and the projected angular distance from the center of the remnant, only the inclination angle of the nearly freely moving knot's velocity vector against the line of sight needs to be constrained in order to estimate the distance. There are ejecta-dominated regions projected close to the outermost boundary of the main shell (e.g., N7) and even beyond it (Ear2). These knots show smaller expansion indices (i.e., stronger deceleration) than N2, while N2 has an apparent nearly constant proper motion since the explosion, and unusually high v_r. The forward shock itself has significantly decelerated: Vink (2008) and Katsuda et al. (2008) found an average expansion parameter of ~0.5–0.6. Hence, it seems likely that N2 may have reached near or even beyond the main shell, similar to ejecta "bullets" reported in other SNRs (e.g., Strom et al. 1995; Park et al. 2012; Winkler et al. 2014).

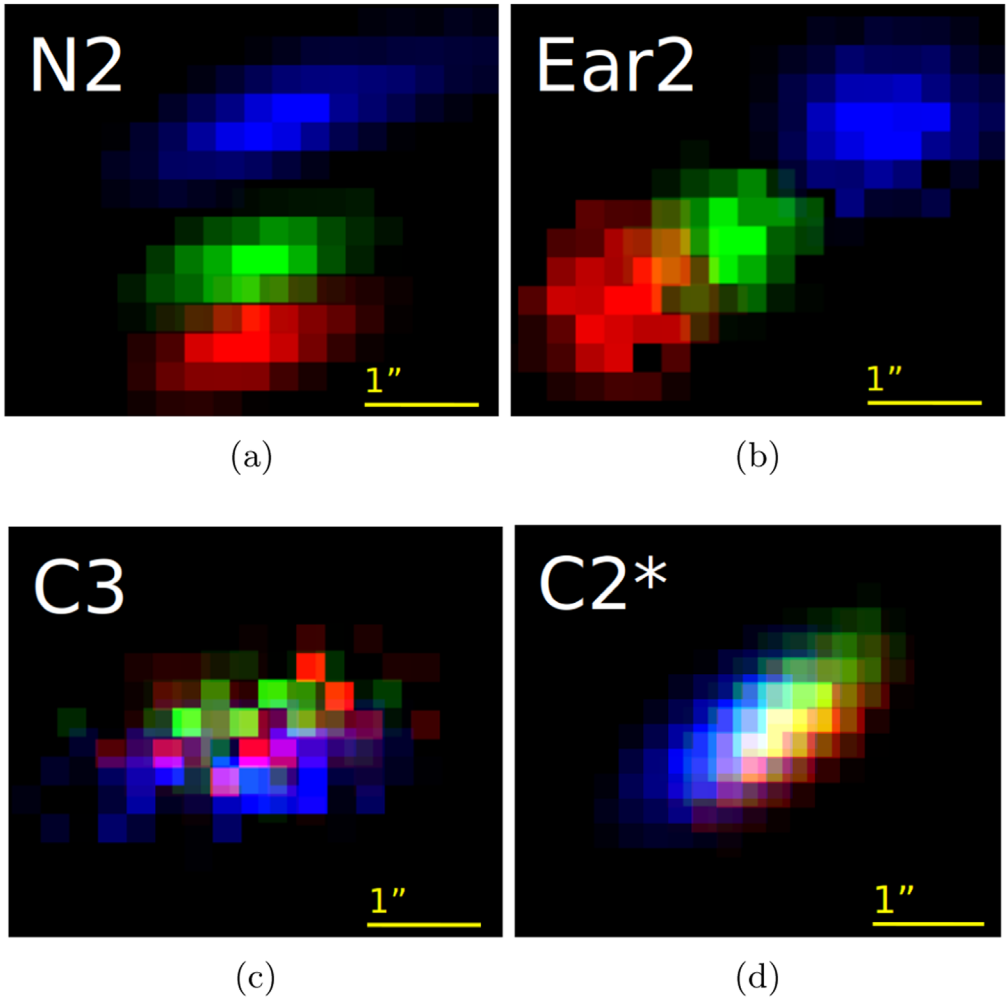

Figure 5. ΔC (where ΔC is the difference between the C statistic for this image and the minimum C statistic, as defined in Section 3.4) images showing positional differences of regions (a) N2, (b) Ear2, (c) C3, and (d) C2* among observations performed in 2000 (red), 2004 (green), and 2014 (blue).

Depending on the location of N2, the inclination angle for its space velocity vector against the line of sight may be constrained. We assume three cases for the physical location of N2: (1) at the outermost boundary of the SNR's main shell (the projected angular distance from the SNR center $D \sim$ 1.′8), (2) at the physical distance corresponding to the angular distance (from the SNR center) to the western Ear's outermost boundary, i.e., the visible maximum angular extent of the X-ray emission ($D \sim$ 2.′3), and (3) a location significantly beyond the main SNR shell at the distance corresponding to ∼1.5 times the radius of the SNR's main shell ($D \sim$ 2.′7). The expansion center of Kepler's SNR has been estimated in radio wavelengths by Matsui et al. (1984) and DeLaney et al. (2002), and later in X-rays by Katsuda et al. (2008) and Vink (2008). Recently, Sato & Hughes (2017b) estimated two possible expansion centers by tracing back the proper motion of a few ejecta knots with high expansion indices to a common origin, one assuming no deceleration, and the other a power-law evolution of radius with time (i.e., deceleration). We take the "decelerated" kinematic center estimated by Sato & Hughes (2017b) as the explosion site unless otherwise noted. We may calculate the distance to Kepler by considering that N2 has been moving with our measured v_r along the line of sight since the explosion. This approach would almost certainly result in an underestimate of the true distance; however, since we are in general more interested in a lower limit to the distance, this assumption would not affect our conclusions.

In scenarios 1, 2, and 3, we assume that N2 has reached the main shell of the remnant, or beyond, thus we estimate distances of $d \sim 7.5$ kpc, ∼5.4 kpc, and ∼4.4 kpc, respectively. Recently, Ruiz-Lapuente (2017) interpreted historical light curves of SN 1604, and Sankrit et al. (2016) used proper motion and line width measurements of Balmer filaments to independently estimate a distance range, $d \sim 5.1 \pm 0.8$ kpc to Kepler. Our distance range is generally consistent with this value, and also with somewhat farther distance estimates that suggest an energetic Type Ia explosion for SN 1604 (Aharonian et al. 2008; Vink 2008; Chiotellis et al. 2012; Patnaude et al. 2012; Katsuda et al. 2015). Considering the amount of ^{56}Ni required to explain the bulk properties of the X-ray spectrum, the spectral and hydrodynamical fitting done by Patnaude et al. (2012) and Katsuda et al. (2015) suggests that the data are incompatible with a normal Type Ia explosion, but may be consistent with a DDTa model, which is more energetic. Since the age is known, this places the SNR at a distance of >5 kpc. However, Ruiz-Lapuente (2017) argue that the best-fit stretch factor to the historical light curve indicates that it is more consistent with a normal SN Ia. Considering that our estimated lower limit (scenario 3) is likely conservative, and unless we have a relatively unique viewing angle, it is reasonable that knot N2 is located nearby, or less than, a distance from the center

of the remnant described in scenario 2. Thus, we may conclude that our v_r measurement suggests $d \gtrsim 5$ kpc, and hence tends to favor the distance estimates, which suggest an energetic Type Ia explosion for SN 1604.

Although it may not be favored due to our measured high proper motion and v_r, for completeness, we may consider that even the fastest ejecta knots (e.g., N2) in Kepler have been significantly decelerated rather than nearly freely expanding. In this scenario, the ejecta knot is heated between the forward and reverse shocks as expected by standard SNR dynamics (Chevalier 1982), and it would be traveling generally with the bulk of ejecta gas in the SNR. With this configuration, a longer distance to Kepler is implied ($d \sim 11.0$ kpc), which we may consider to be a conservative upper limit.

4.2. Velocity Distribution of Ejecta

Based on our v_r and proper motion measurements, we measure space velocities, $v_s \sim (1100–8700)d_6$ km s^{-1} (with d_6 in units of 6 kpc), with an average velocity, $v_s \sim 4600d_6$ km s^{-1}, for the 15 individual ejecta knots. The fastest known stars in the Milky Way (which are probably ejected from SN explosions in white dwarf binaries) show space velocities of $\sim$2000 km s^{-1} (Shen et al. 2018). Thus, the velocities we obtain for several knots are highly significant, and cannot be attributed to a systemic velocity for the SNR.

The broad range of ejecta space velocities and expansion indices (see Table 1) that we measure in our sample may be characteristic for an SNR transitioning from the free-expansion phase to the Sedov–Taylor phase. Measurements of the proper motion at various locations along Kepler's forward shock by Katsuda et al. (2008) and Vink (2008) found expansion indices of 0.47–0.82 and 0.3–0.7, respectively. For remnants nearing the Sedov–Taylor phase, Chevalier (1982) estimated $\eta = 0.4$ for $s = 0$ and $\eta = 0.67$ for $s = 2$ ambient density power-law solutions. Hence, our ejecta velocity measurements and previous forward shock analyses apparently suggest that the kinematics for some regions in Kepler may be dominated by nearly free expansion, while others are better described by Sedov–Taylor dynamics. New 3D hydrodynamical simulations that focus on Kepler and these high η knots may give some insight into their origin.

The knots N2, N5, N1, and N3 have the highest measured space velocities (6100–8700d_6 km s^{-1}), and are all located in the "steep arc" (DeLaney et al. 2002) of Kepler's SNR, a "bar" of bright X-ray emission that runs from east to west, located about halfway between the center of the remnant and the outer edge of the main shell. They are projected close to each other within a small ($50'' \times 20''$) area. This proximity, and similarities in their measured Si abundances, space velocity vectors, and expansion indices, suggest that these knots might have originated generally from a "common" layer of the exploding white dwarf. Sato & Hughes (2017b) measured properties of another knot (they label "N4") projected within the steep arc, which exhibited similar properties to N2, N5, N1, and N3. This suggests that ejecta within the steep arc have generally homogeneous kinematic and spectroscopic properties.

In the western Ear, we measure high space velocity in region Ear2, $v_s \sim 5800d_6$ km s^{-1}. Such a high velocity may be expected considering the knot's projected location in the western Ear feature, which protrudes out about 30% beyond the main shell. Interestingly, knot Ear1 has a significantly smaller space velocity, $v_s \sim 3300d_6$ km s^{-1}, even though it is projected very close to the position of Ear2. Knot Ear1 may be interacting with a CSM-dominated feature identified by Burkey et al. (2013) projected adjacent to it, which could have caused it to significantly decelerate recently. Such an interaction between ejecta and CSM may produce Hα emission. We searched for Hα emission at the location of Ear1 in the archival Hubble Space Telescope images (with the F656N filter) of Kepler (Sankrit et al. 2016). We found a faint wisp centered at Ear1's position, possibly indicating the presence of shocked CSM gas, which would support our conclusion of an ejecta-CSM interaction there.

Considering their spatial proximity and similarly high Si abundance, it seems likely that Ear1 and Ear2 were produced very near each other during the SN. It is interesting that these knots are projected $\sim 1'$ in decl. north of the center of the remnant, as are the ejecta knots in the steep arc. In our distance estimation, we assumed that knot N2 is located at or beyond the main shell. Thus, if we viewed Kepler at a different angle, it may appear as though the steep arc and western Ear are similar structures extending to different directions. This morphological interpretation may not be consistent with the bipolar-outflow scenario (Tsebrenko & Soker 2013) as the origin of the Ears. However, we measured generally higher Si abundances in the western Ear than in the steep arc (roughly by a factor of $\sim$5), as did Sun & Chen (2019), who recently reported a similar result. This abundance discrepancy is not in line with the scenario that the Ear and arc features share a common physical origin. Thus, while we find intriguing similarities in kinematic properties between these substructures of Kepler, their true physical origins remain unanswered. Detailed hydrodynamic simulations may be needed to test these scenarios, which are beyond the scope of this work.

The HETG spectra of 10 ejecta regions from our sample show a significant Doppler shift (i.e., $|v_r| \gtrsim 10^3$ km s^{-1}). The majority of them (8 regions) are redshifted. This may suggest a significantly asymmetric velocity distribution of ejecta knots along the line of sight (see Figure 6). However, we note that our sample size of the ejecta knots is limited. In particular, our sample regions offer very little coverage in the southern shell of the SNR. Thus, the apparent asymmetric ejecta distribution along the line of sight might have been a selection effect. To make a conclusive statement regarding the overall 3D distribution of Si-rich ejecta in Kepler, a significantly larger sample of high-resolution velocity measurements from ejecta regions across the entire face of the SNR is required. A significantly deeper Chandra HETG observation would be needed to achieve this. Nonetheless, it is interesting to note that some similar uneven ejecta distributions have been reported in studies using the lower-resolution X-ray CCD spectroscopy from archival Chandra ACIS data. Sato & Hughes (2017b) found that only 2 ejecta-dominated knots out of the 11 (4 in common with this work) included in their study were significantly blueshifted. Those regions show relatively weak He-like Si Kα emission line fluxes, thus we could not measure their v_r using our HETGS data due to low photon count statistics. Kasuga et al. (2018) reported that a general asymmetry exists in the Fe-rich ejecta along the line of sight in Kepler. Burkey et al. (2013) suggested that the asymmetry in Fe ejecta across the face of the SNR could be a result of ejecta being blocked by the progenitor's companion star. While our results suggesting an uneven line-of-sight ejecta distribution cannot be conclusive based on the current data, previous studies of Kepler appear to be consistent with our results.

The suggested asymmetric distribution of the ejecta (if it is confirmed) could be the result of Kepler's interactions with its

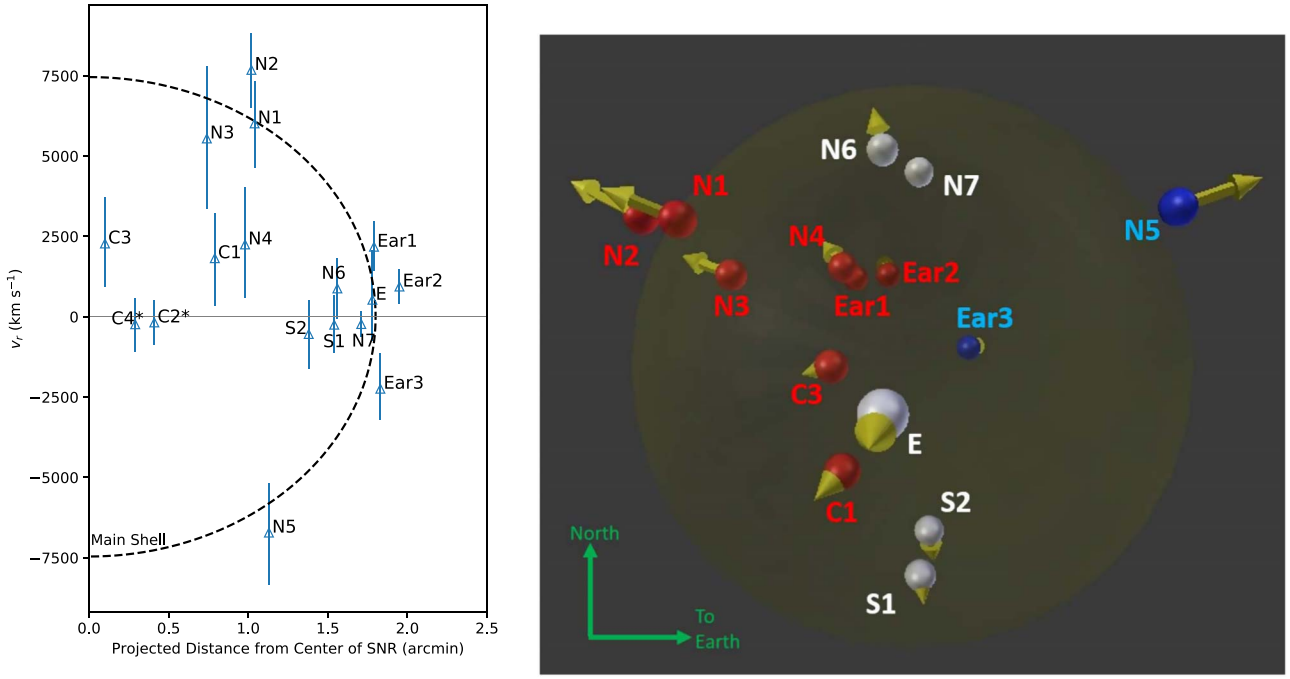

(a) (b)

Figure 6. Panel (a) shows the positions of ejecta knots in v_r vs. r (projected angular distance from the center of the SNR) space. The dashed line is the approximate location of the outermost boundary of the main SNR shell. Panel (b) shows a 3D perspective of the locations of our measured ejecta knots. The red spheres represent redshifted knots, blue spheres are blueshifted knots, and white spheres are those with negligible Doppler shift. The gold arrows indicate the knots' relative magnitude of space velocities and directions. The shaded circle shows the approximate location of the main shell of Kepler's SNR.

nonuniform surroundings. Patnaude et al. (2012) and Blair et al. (2007) argued that the north–south density gradient they found in the surrounding medium of Kepler is required to explain the observed bowshock in the north of the remnant, and the infrared intensity variation between the northern and southern rims. Such a density gradient across the near and far sides of the remnant, with surrounding material on the near side having a lower density on average, could lead to an under-developed or late reverse shock, causing blueshifted knots to appear fainter. Alternatively, the tentative asymmetric ejecta distribution along the line of sight might have been caused by a true asymmetry in the SN explosion itself. The global asymmetry in SNe Ia may in general be caused by the strength and geometry of ignition of the SN explosion (Maeda et al. 2010). The validity and true nature of the asymmetric ejecta distribution in Kepler's SNR that we observe in the Chandra data are unclear due to our small sample size. Follow-up Chandra HETGS observations of Kepler with deeper exposures would be warranted to perform a more extensive census of the ejecta velocity distribution (significantly beyond the capacity of the existing ACIS and HETG data) throughout the entire SNR, which is required to reveal the true 3D nature of Kepler's SN explosion.

5. Conclusions

We have measured the radial velocities and proper motions of 17 small emission features (15 ejecta and 2 CSM knots) in Kepler's supernova remnant using our Chandra HETGS observation and the archival Chandra ACIS data. We find that a handful of knots are moving at speeds approaching $\sim 10^4$ km s^{-1}, with expansion indices approaching $\eta \sim 1$, indicating nearly a free expansion. Based on our radial velocity measurement of such a fast-moving ejecta knot, we estimate the distance to Kepler. While our distance estimates may vary depending on our assumption of the degree of deceleration of the ejecta knot ($d \sim 4.4$–7.0 kpc), a relatively long distance of $d > 5$ kpc is favored. Our estimated distance range generally supports an energetic SN Ia for Kepler.

We note that most of our v_r measurements indicate a redshifted spectrum, suggesting an asymmetry along the line-of-sight ejecta distribution of the remnant. However, this study involves only a small sample of ejecta knots, most of which are projected in the northern shell of the SNR. Thus, while it provides hints into some intriguing kinematic characteristics of the SN Ia explosion that created Kepler, this work is limited in revealing the true 3D structure of the entire SNR. A longer observation of Kepler using the Chandra HETGS would be required to measure v_r for a significantly larger number of ejecta knots covering the entire face of the SNR. Such measurements would yield a detailed picture of the 3D distribution of ejecta, and provide observational constraints for more realistic SN Ia models.

This work has been supported in part by NASA Chandra grants GO6-17060X and AR7-18006X. J.P.H. acknowledges support for supernova remnant research from NASA grant NNX15AK71G to Rutgers University. T.S. was supported by the Japan Society for the Promotion of Science (JSPS) KAKENHI grant No. JP19K14739 and the Special Postdoctoral Researchers Program in RIKEN. We also thank the anonymous referees for providing valuable input that strengthened this paper.

Appendix

A.1. Line Emission Ratios

To determine the line-emission contributions from electronic shell transitions of Si XIII and Si XII, we measured the temperature and ionization timescale of each knot by fitting an absorbed plane shock model to its broadband (0.3–7.0 keV) ACIS spectrum (see Section 3.3). We show our results in Table A1. Based on each knot's best-fit temperature and

Table A1
ACIS Spectral Fitting Results

Region	kT (keV)	τ (10^{10} s cm^{-3})[a]	Redshift (10^{-2})	K (10^{8} cm^{-5})[b]	χ^2/dof	i/r[c]	f/r[d]
N2	$3.86^{+0.94}_{-0.75}$	$2.18^{+0.28}_{-0.23}$	$2.66^{+0.07}_{-0.22}$	$12.8^{+2.2}_{-1.9}$	191.2/138	0.06	0.67
N1	$2.15^{+0.41}_{-0.33}$	$2.32^{+0.30}_{-0.26}$	$2.47^{+0.01}_{-0.28}$	$9.99^{+2.06}_{-1.46}$	131.9/103	0.10	0.64
N3	$3.49^{+0.69}_{-0.59}$	$2.16^{+0.17}_{-0.04}$	$2.13^{+0.07}_{-0.08}$	$10.4^{+1.2}_{-1.0}$	135.8/113	0.06	0.67
C3	$2.44^{+0.49}_{-0.42}$	$0.99^{+0.22}_{-0.14}$	$0.15^{+0.05}_{-0.05}$	$8.27^{+1.04}_{-1.02}$	120.3/108	0.10	1.77
N4	$4.49^{+2.25}_{-0.72}$	$1.85^{+0.36}_{-0.29}$	$1.08^{+0.10}_{-0.01}$	$4.47^{+0.33}_{-0.25}$	144.9/104	0.05	0.85
Ear1	$0.56^{+0.02}_{-0.04}$	$78.2^{+54.6}_{-19.2}$	$1.61^{+0.08}_{-0.05}$	$5.78^{+1.14}_{-0.48}$	135.8/103	0.22	0.59
C1	$3.64^{+1.03}_{-0.69}$	$2.11^{+0.28}_{-0.21}$	$0.31^{+0.04}_{-0.01}$	$4.76^{+0.64}_{-0.66}$	145.2/109	0.06	0.69
Ear2	$2.39^{+0.52}_{-0.38}$	$1.08^{+0.06}_{-0.12}$	$0.74^{+0.03}_{-0.04}$	$4.81^{+1.15}_{-0.57}$	114.1/112	0.10	1.58
N6	$3.34^{+0.88}_{-0.87}$	$2.58^{+0.52}_{-0.22}$	$0.80^{+0.01}_{-0.18}$	$3.07^{+0.40}_{-0.39}$	135.9/98	0.07	0.55
E	$3.05^{+0.39}_{-0.30}$	$1.52^{+0.27}_{-0.09}$	$1.06^{+0.01}_{-0.26}$	$29.3^{+1.6}_{-2.6}$	159.0/137	0.08	1.03
C2*	$1.27^{+0.12}_{-0.11}$	$5.15^{+1.34}_{-0.77}$	$0.19^{+1.10}_{-0.18}$	$29.8^{+2.8}_{-1.2}$	115.8/109	0.14	0.47
N7	$0.80^{+0.01}_{-0.02}$	$73.5^{+14.9}_{-11.2}$	$0.14^{+0.01}_{-0.17}$	108^{+7}_{-5}	194.9/143	0.19	0.51
C4*	$0.80^{+0.06}_{-0.07}$	$12.5^{+2.6}_{-2.4}$	$-0.33^{+0.02}_{-0.08}$	$97.1^{+8.4}_{-9.1}$	165.2/119	0.19	0.52
S1	$2.16^{+0.63}_{-0.59}$	$1.08^{+0.18}_{-0.12}$	$-0.49^{+0.12}_{-0.01}$	$1.38^{+0.53}_{-0.24}$	126.1/92	0.10	1.56
S2	$0.53^{+0.02}_{-0.02}$	300^{+1590}_{-131}	$-0.50^{+0.03}_{-0.04}$	$11.4^{+1.9}_{-0.3}$	137.0/107	0.23	0.61
Ear3	$4.02^{+1.73}_{-1.04}$	$0.94^{+0.12}_{-0.09}$	$-1.18^{+0.05}_{-0.11}$	$3.36^{+0.35}_{-0.66}$	139.9/107	0.07	2.15
N5	$4.93^{+1.84}_{-1.32}$	$1.16^{+0.12}_{-0.13}$	$-1.68^{+0.06}_{-0.02}$	$4.02^{+1.04}_{-1.02}$	146.4/113	0.05	1.68

Notes.
[a] $\tau = n_e t$, where n_e is the electron density, and t is the time since the plasma was shocked.
[b] $K = \int n_e n_{\rm H} dV / 4\pi d^2$, where $n_{\rm H}$ is the hydrogen density, V is the volume of the region, and d is the distance to the region.
[c] Si Kα intercombination (i) to resonance (r) line ratio.
[d] Si Kα forbidden (f) to resonance line ratio.

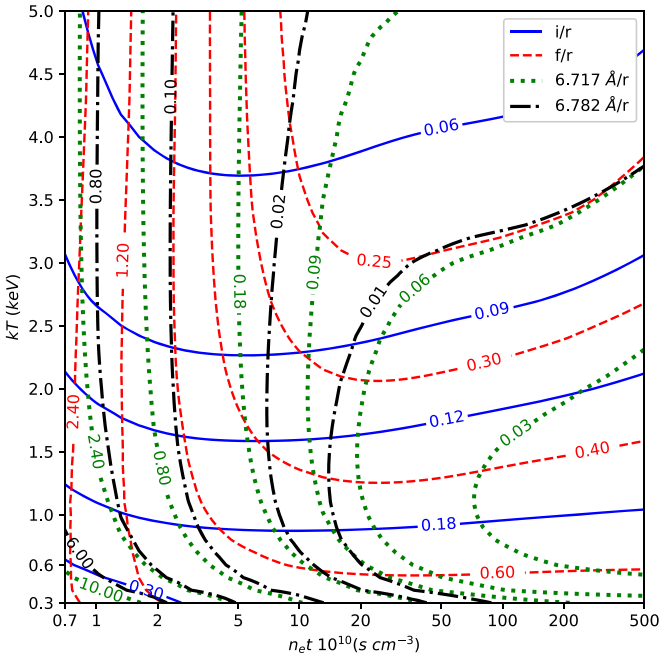

Figure A1. Contours of line-emission ratios for various temperatures and ionization timescales. The blue solid and red dashed contours represent ratio values of of Si XIII intercombination to resonance, and forbidden to resonance line fluxes, respectively. The green dotted and black dashed–dotted contours show ratio values of Si XII emission lines 6.717 and 6.782 Å, to the Si XIII resonance line (r), respectively.

ionization timescale, we used a `phabs*vvpshock` model to calculate the line ratios using XSPEC (version 12.10) with NEI APEC spectral data (version 3.0.9) (Arnaud 1996; Smith et al. 2001). Our best-fit ACIS broadband models (see Section 3.3) suggest ratio values ranging from ∼0.05–0.23 and 0.47–2.15 for i/r and f/r, respectively. The 6.717 and 6.782 Å Si XII line ratios vary from 0.03 to 1.96 and 8e–4–0.98, respectively. Figure A1 shows contour plots of each line ratio for a range of temperatures and ionization timescales. Varying the line ratio values used in each measurement does not significantly affect our main results for the high v_r knots (N1–N3, N5), and although our sample size is limited, the overall dominance of the redshift in the ejecta v_r also does not change. Hence, the overall results of our HETG v_r measurements are generally independent of the line ratio values estimated from the ACIS model fits.

ORCID iDs

Matthew J. Millard https://orcid.org/0000-0001-7106-8502
Jayant Bhalerao https://orcid.org/0000-0002-9312-7937
Sangwook Park https://orcid.org/0000-0003-3900-7739
Toshiki Sato https://orcid.org/0000-0001-9267-1693
John P. Hughes https://orcid.org/0000-0002-8816-6800
Patrick Slane https://orcid.org/0000-0002-6986-6756
Daniel Patnaude https://orcid.org/0000-0002-7507-8115
David Burrows https://orcid.org/0000-0003-0729-1632
Carles Badenes https://orcid.org/0000-0003-3494-343X

References

Aharonian, F., Akhperjanian, A. G., Barres de Almeida, U., et al. 2008, A&A, 488, 219
Arnaud, K. A. 1996, in ASP Conf. Ser. 101, Astronomical Data Analysis Software and Systems V, ed. G. H. Jacoby & J. Barnes (San Francisco, CA: ASP), 17
Badenes, C., Hughes, J. P., Bravo, E., & Langer, N. 2007, ApJ, 662, 472
Bhalerao, J., Park, S., Dewey, D., et al. 2015, ApJ, 800, 65
Blair, W. P., Ghavamian, P., Long, K. S., et al. 2007, ApJ, 662, 998
Blair, W. P., Long, K. S., & Vancura, O. 1991, ApJ, 366, 484
Borkowski, K. J., Lyerly, W. J., & Reynolds, S. P. 2001, ApJ, 548, 820

Burkey, M. T., Reynolds, S. P., Borkowski, K. J., & Blondin, J. M. 2013, ApJ, 764, 63
Cash, W. 1979, ApJ, 228, 939
Chevalier, R. A. 1982, ApJL, 259, L85
Chiotellis, A., Schure, K. M., & Vink, J. 2012, A&A, 537, A139
Davis, J. E., Bautz, M. W., Dewey, D., et al. 2012, Proc. SPIE, 8443, 84431A
DeLaney, T., Koralesky, B., Rudnick, L., & Dickel, J. R. 2002, ApJ, 580, 914
Dennefeld, M. 1982, A&A, 112, 215
Drake, G. W. 1988, CaJPh, 66, 586
Foight, D. R., Güver, T., Özel, F., & Slane, P. O. 2016, ApJ, 826, 66
Fruscione, A., McDowell, J. C., Allen, G. E., et al. 2006, Proc. SPIE, 6270, 62701V
Hachisu, I., Kato, M., & Nomoto, K. 2008, ApJ, 679, 1390
Houck, J. C., & Denicola, L. A. 2000, in ASP Conf. Ser. 216, Astronomical Data Analysis Software and Systems IX, ed. N. Manset, C. Veillet, & D. Crabtree (San Francisco, CA: ASP), 591
Hoyle, F., & Fowler, W. A. 1960, ApJ, 132, 565
Huenemoerder, D. P., Mitschang, A., Dewey, D., et al. 2011, AJ, 141, 129
Hwang, U., Hughes, J. P., & Petre, R. 1998, ApJ, 497, 833
Iben, I., Jr., & Tutukov, A. V. 1984, ApJS, 54, 335
Kasen, D., Röpke, F. K., & Woosley, S. E. 2009, Natur, 460, 869
Kasuga, T., Sato, T., Mori, K., Yamaguchi, H., & Bamba, A. 2018, PASJ, 70, 88
Katsuda, S., Mori, K., Maeda, K., et al. 2015, ApJ, 808, 49
Katsuda, S., Tsunemi, H., Uchida, H., & Kimura, M. 2008, ApJ, 689, 225
Lazendic, J. S., Dewey, D., Schulz, N. S., & Canizares, C. R. 2006, ApJ, 651, 250
Maeda, K., Benetti, S., Stritzinger, M., et al. 2010, Natur, 466, 82
Maeda, K., Leloudas, G., Taubenberger, S., et al. 2011, MNRAS, 413, 3075
Martínez-Rodríguez, H., Badenes, C., Lee, S.-H., et al. 2018, ApJ, 865, 151
Matsui, Y., Long, K. S., Dickel, J. R., et al. 1984, ApJ, 287, 295
McKee, C. F., & Ostriker, J. P. 1977, ApJ, 218, 148
Park, S., Badenes, C., Mori, K., et al. 2013, ApJL, 767, L10
Park, S., Hughes, J. P., Slane, P. O., et al. 2012, ApJ, 748, 117
Patnaude, D. J., Badenes, C., Park, S., & Laming, J. M. 2012, ApJ, 756, 6
Post, S., Park, S., Badenes, C., et al. 2014, ApJL, 792, L20
Ruiz-Lapuente, P. 2017, ApJ, 842, 112
Sankrit, R., Blair, W. P., Delaney, T., et al. 2005, AdSpR, 35, 1027
Sankrit, R., Raymond, J. C., Blair, W. P., et al. 2016, ApJ, 817, 36
Sato, T., & Hughes, J. P. 2017a, ApJ, 840, 112
Sato, T., & Hughes, J. P. 2017b, ApJ, 845, 167
Sato, T., Katsuda, S., Morii, M., et al. 2018, ApJ, 853, 46
Shen, K. J., Boubert, D., Gänsicke, B. T., et al. 2018, ApJ, 865, 15
Smith, R. K., Brickhouse, N. S., Liedahl, D. A., et al. 2001, ApJL, 556, L91
Strom, R., Johnston, H. M., Verbunt, F., et al. 1995, Natur, 373, 590
Sun, L., & Chen, Y. 2019, ApJ, 872, 45
Tsebrenko, D., & Soker, N. 2013, MNRAS, 435, 320
Uchida, H., Yamaguchi, H., & Koyama, K. 2013, ApJ, 771, 56
Vink, J. 2008, ApJ, 689, 231
Wang, C.-Y., & Chevalier, R. A. 2001, ApJ, 549, 1119
Williams, B. J., Borkowski, K. J., Reynolds, S. P., et al. 2012, ApJ, 755, 3
Wilms, J., Allen, A., & McCray, R. 2000, ApJ, 542, 914
Winkler, P. F., Williams, B. J., Reynolds, S. P., et al. 2014, ApJ, 781, 65
Yamaguchi, H., Hughes, J. P., Badenes, C., et al. 2017, ApJ, 834, 124